Visualizing cellular and tissue ultrastructure using Ten-fold Robust Expansion Microscopy (TREx)

Hugo G.J. Damstra[1], Boaz Mohar[2], Mark Eddison[2], Anna Akhmanova[1], Lukas C. Kapitein[1*], Paul W. Tillberg[2*]

[1]Cell Biology, Neurobiology and Biophysics, Department of Biology, Faculty of Science, Utrecht University, Utrecht, The Netherlands

[2]Janelia Research Campus, HHMI, Ashburn, Virginia 20147, USA

Correspondence: l.kapitein@uu.nl; tillbergp@janelia.hhmi.org

ABSTRACT

Expansion microscopy (ExM) is a powerful technique to overcome the diffraction limit of light microscopy that can be applied in both tissues and cells. In ExM, samples are embedded in a swellable polymer gel to physically expand the sample and isotropically increase resolution in x, y and z. The maximum resolution increase is limited by the expansion factor of the polymer gel, which is four-fold for the original ExM protocol. Variations on the original ExM method have been reported that allow for greater expansion factors, for example using iterative expansion, but at the cost of ease of adoption or versatility. Here, we systematically explore the ExM recipe space and present a novel method termed Ten-fold Robust Expansion Microscopy (TREx) that, like the original ExM method, requires no specialized equipment or procedures to carry out. We demonstrate that TREx gels expand ten-fold, can be handled easily, and can be applied to both thick tissue sections and cells enabling high-resolution subcellular imaging in a single expansion step. We show that applying TREx on antibody-stained samples can be combined with off-the-shelf small molecule stains for both total protein and membranes to provide ultrastructural context to subcellular protein localization.

INTRODUCTION

Expansion Microscopy (ExM) circumvents the diffraction limit of light microscopy by physically expanding the specimen four-fold in each dimension (Chen, Tillberg and Boyden, 2015; Tillberg *et al.*, 2016). While other super-resolution approaches require specialized optics (Hell and Wichmann, 1994), fluorophores (Rust, Bates and Zhuang, 2006), or software (Gustafsson, 2000), and are not readily compatible with thick tissue slices, ExM is compatible with any microscope (Zhang *et al.*, 2016; Gao *et al.*, 2019), including combinations with other super resolution modalities (Halpern *et al.*, 2017; Gao *et al.*, 2018; Xu *et al.*, 2019), and performs well in both cultured cells and thick tissue slices (Chen, Tillberg and Boyden, 2015; Tillberg *et al.*, 2016). The resolution increase of ExM depends on labeling efficiency, anchoring efficiency, and the expansion factor of the gel recipe used. Recently, method variants have been described that increase the expansion factor to increase the maximum resolution obtainable with ExM. For example, iterative ExM (iExM) uses sequential embedding in multiple expansion gels to achieve 15x and greater expansion but requires a complex sequence of gel re-embedding, link cleaving, and fluorophore transfer (Chang *et al.*, 2017), limiting broad adoption in biological labs.

The expansion factor of the gel itself can be increased by decreasing the concentration of crosslinker (Okay, 2009), usually bisacrylamide (bis), at the expense of gel mechanical integrity. For example, reducing the bis in the original ExM recipe from 1.5 ppt (parts per thousand) to 250 ppm (parts per million) produces a ~9x expanding gel (Chen, Tillberg and Boyden, 2015, SF5), but these gels are too soft to hold their shape under the force of gravity. As a result, they are difficult to handle without breaking and display non-uniform expansion. This tradeoff of expansion versus gel mechanical integrity has not been explored in a quantitative or systematic way.

Another gel recipe variant, using a high concentration of the monomer dimethylacrylamide (DMAA), has enough crosslinking through side reactions and polymer chain entanglement that the crosslinker can be omitted entirely, producing ~10-fold expansion in one step (Truckenbrodt *et al.*, 2018). This recipe has been used to expand cultured cells and thin cryosectioned tissue (Truckenbrodt *et al.*, 2019), but this recipe reportedly requires rigorous degassing to remove oxygen prior to gelation, making it laborious to adopt. Moreover, expansion of >50 µm thick tissue slices has not been demonstrated using this method. Thus, a robustly validated and easily adoptable method that is compatible with multiple sample types and enables single step expansion well over 4x without compromising gel integrity is lacking.

Here, we explored the expansion gel recipe space in a systematic manner, assessing the limits of single-round expansion using reagents and methods that would be familiar to labs already doing standard ExM. For any given choice of recipe parameters (monomer concentrations, gelation temperature, radical

initiation rate, etc.), varying the crosslinker alone yielded a family of recipes whose expansion factor and mechanical quality vary smoothly from high expanding, poor quality to low expanding, excellent quality gels. A range of crosslinker concentrations was tested because the optimal crosslinker concentration may be different for each recipe family. Here we present an optimized ExM method that allows for robust ten-fold expansion in a single step, termed TREx. We show TREx can be used to expand thick tissue slices and adherent cells and is compatible with antibodies, as well as off-the-shelf small molecule stains for total protein and membranes. Together, we show how TREx enables 3D nanoscopic imaging of specific structures stained with antibodies in combination with cellular ultrastructure.

RESULTS

To systematically explore the expansion recipe space, we developed a streamlined method for synthesizing dozens of gel recipes and characterizing their mechanical quality in parallel. For every set of gel recipe parameters (component concentrations and gelation temperature, listed in Fig. 1A) we define a recipe family as the set of recipes generated by varying the crosslinker (bisacrylamide) concentration. For each family, we tested five recipes with crosslinker concentrations log-spaced from 1 ppt (parts per thousand or mg/mL) to 10 ppm (parts per million), plus one with zero crosslinker. We also included the original ExM recipe, with 1.5 ppt crosslinker. For each recipe, we cast three gel specimens, expanded them fully in water, and measured the expansion factor (Fig. 1B). We found that resistance to deformation under the force of gravity was a good proxy for the more subjective judgement of ease of gel handling. We measured gel deformation by placing a semicircular punch from each gel upright on its curved edge and allowing the gel corners to deflect under the force of gravity. We defined the deformation index as the vertical displacement of each gel corner, divided by the gel radius (Fig. 1C), which ranges from 0 (for gels that do not deform) to 1 (for gels that deform freely under their own weight). We manually calibrated this measurement, finding that deformation indices between 0 and 0.125 corresponded to gels with excellent ease of handling, 0.125 to 0.25 corresponded to acceptable ease of handling, and anything higher than 0.25 was unacceptable. While not as theoretically informative as elastic modulus and yield strength measurements, this measurement can be repeated and extended to new gel recipes by any lab developing expansion methods, without access to specialized equipment. We plotted the deformation index for each gel as a function of its expansion factor (Fig. 1D).

Development of the TRex gel recipe

We began by characterizing a recipe family generated from the original ExM recipe (family A). Consistent with (Chen, Tillberg and Boyden, 2015), reducing the crosslinker to 300 ppm increased the expansion to ~9x, below which the gels fail to form consistently (Fig. 1B, purple). We next characterized a

high-monomer recipe family adapted from the 4x-expanding Ultra-ExM recipe (Gambarotto *et al.*, 2019) (family B). Gambarotto et al found that a higher monomer concentration relative to the original ExM recipe was necessary for high fidelity preservation of the shape of centrioles. This was offset with a lower crosslinker concentration of 1 ppt bisacrylamide to achieve 4x expansion. Indeed, for this high-monomer family of recipes, expansion as a function of crosslinker concentration was shifted leftward compared to standard ExM (Fig. 1B, blue). As the crosslinker was decreased below 30 ppm the increase in expansion factor saturated around 11.5x. The deformation index versus expansion factor curve for the high monomer family ran below that for standard ExM, indicating that for a given expansion factor a high-monomer gel holds its shape better than the corresponding standard ExM gel (Fig. 1D, blue).

Compared with standard ExM, this high monomer family uses a higher concentration of radical initiator and accelerator to trigger polymerization (5 ppt each of APS and TEMED, versus 2 ppt in standard ExM), which causes gels to form within minutes at room temperature. Because the rates of initiation and polymerization increase with temperature, it is likely that specimens are not fully equilibrating to the gelation temperature of 37 °C before the onset of gelation, introducing a potential source of experimental variability. This rapid gelation makes the gelation chamber assembly step more time sensitive and presents challenges for adapting the technique to thick tissue slices, as thick tissue slices require extra time for the gelation solution to diffuse throughout the sample prior to polymerization. We tested the same high monomer recipe family but with initiator reduced to 1.5 ppt (family C). For all families, the accelerator (TEMED) was varied in tandem with the initiator. The expansion versus crosslinker curve for this family was similar to family B for high crosslinker concentrations but displayed a slightly greater slope. Unlike family B, the expansion factor did not saturate upon decreasing the crosslinker concentration. Instead, the expansion factor continued to increase to 13x expansion at 10ppm crosslinker (Fig. 1B, red), with gels failing to form without any crosslinker present. While deformation of these gels for the same expansion factor was increased compared to family B, although better than for family A and acceptable up to an expansion factor of 10 (30 ppm bis, Fig. 1D, red), in our judgement this was outweighed by the slower and more controlled gelation kinetics achieved by lowering the concentration of initiator and accelerator.

The recipe families explored above (B, C) feature a high fraction of sodium acrylate relative to acrylamide. Acrylate drives expansion of the gel but comes in widely varying purity levels and, we found in some cases, causes tissue to shrink. The tissue shrinkage was modest compared to the gel expansion but may not be uniform at all scales. We therefore tested an alternative recipe family (D) with higher acrylamide to acrylate ratio (2.1:1). Increasing the acrylamide to acrylate ratio did not change the expansion factors appreciably at a given crosslinker concentration, suggesting that the swelling effect of acrylate saturates at

119 high concentrations. At the maximum expansion factor of ~10, the deformation behavior was comparable
120 to family C, which biased our choice to family D due to the lower acrylate content of the gels.

121 We further tested an elevated gelation temperature of 50 °C (family E), in an attempt to increase
122 the initiation rate without introducing premature gelation at room temperature seen in recipe family B.
123 Compared to family D, the expansion factors were around 15% higher at 100 ppm (6x) and 300 ppm
124 crosslinker (9x), but gelation failed at lower concentrations, leaving family D as the family with a higher
125 maximum expansion factor (i.e., 10x at 30 ppm bis). The deformation versus expansion curve for family E
126 was similar to the other high monomer recipe families (Fig. 1D, green), but was found to be sensitive to
127 processing details, such as the gelation chamber construction and placement within the incubator. This
128 suggests that premature gelation prior to equilibrating at the higher temperature reduces the replicability of
129 this recipe family.

130 Considering all 5 recipe families, family B (high acrylate and high APS/TEMED) displayed the
131 best mechanical performance, i.e. the lowest deformation index for any given expansion factor. Family D
132 (high acrylamide and low APS/TEMED) displayed similar performance, with the deformation index
133 remaining well within the acceptable range for expansion factors up to 10. In handling high-expanding
134 (>8x) gels from all recipe families, we found that while those from the standard ExM family (A) were
135 extremely prone to breaking, those from any of the high monomer families could be handled more easily
136 (and even dropped from a height of several feet) without breaking. Because the reduced initiator
137 concentration of family D results in a slower and more controlled polymerization rate, and because we
138 preferred a lower acrylate content, we chose this recipe family to proceed to biological specimen expansion.
139 We found that the exact expansion factor varied for different gelation chamber geometries but could readily
140 be adjust by finetuning the crosslinker concentration (e.g., 50 ppm for Ashburn, VA, USA experiments
141 versus 90 ppm for Utrecht, The Netherlands experiments), We thus recommend that users test gels with a
142 range of crosslinker concentrations between 30 and 100 ppm to find a suitable recipe for their specimen
143 preparation. We name the resulting method Ten-fold Robust Expansion (TREx) microscopy.

144 **Subcellular imaging of specific proteins and cellular ultrastructure in thick brain slices**

145 A major advantage of ExM over other super-resolution techniques is its compatibility with thick
146 tissue slices. Tissue slices require the onset of gelation to be delayed, usually with low temperature
147 incubation and a radical inhibitor (e.g. 4-Hydroxy-TEMPO; 4HT), to give the monomer solution time to
148 diffuse into the tissue (Chen, Tillberg and Boyden, 2015; Tillberg *et al.*, 2016) . For TREx, we found that
149 in some conditions room oxygen was sufficient to inhibit gelation with shaking on ice indefinitely. To
150 increase robustness for thick tissue slices, we included 15 ppm 4HT, allowing ample time to mount

151 specimens in gelation chambers at room temperature. ExM enables uniform expansion by treating
152 embedded tissue with strong proteolytic digestion step. Proteins (including antibodies) are crosslinked to
153 the gel with acryloyl-X SE (AcX), allowing for retention of protein fragments after digestion. Replacing
154 proteolytic digestion with a high detergent, high temperature disruption step has been shown to enable
155 expansion with better overall retention of proteins (Ku *et al.*, 2016; Tillberg *et al.*, 2016; Gambarotto *et al.*,
156 2019; Zwettler *et al.*, 2020). We found that this gentler disruption approach also allowed the AcX anchor
157 treatment to be reduced from 100 µg/mL overnight (standard ExM) to 10 µg/mL for 1 hour while enabling
158 full expansion of mouse brain slices without the appearance of crack-like artifacts.

159 In electron microscopy, non-specific stains for proteins and membranes are commonly used to
160 provide structural detail at high spatial resolution. Recently, the use of non-specific NHS ester protein stains
161 and other small molecule probes has been combined with ExM (M'Saad and Bewersdorf, 2020; Mao *et al.*,
162 2020; Yu *et al.*, 2020). Expansion allows visualization of intracellular detail in densely stained samples,
163 which would not otherwise lead to meaningful contrast. These applications have the promise to bring
164 together the advantages of light microscopy (specific staining using antibodies and volumetric imaging)
165 with the advantage of seeing cellular context typically provided by electron microscopy. Because TREx
166 reaches single-step expansion factors at which small-molecule stains are expected to be useful, we set out
167 to explore this idea further. We applied NHS ester dyes to demonstrate total protein content in thick slices
168 (100 µm) of mouse brain cortex expanded with TREx (Fig. 2A and Supp. Movie 1). The neuropil region
169 outside the cell somas contained a rich profusion of fibers and structures visible in sharp relief. The nucleus
170 of each cell was easily identified, with especially strong staining in nucleoli-like structures. Surrounding
171 each nucleus, the nuclear envelope could be identified, with particularly dense total protein stain on the side
172 facing the nucleus. The nuclear envelope was punctuated by heavily stained spots that span the envelope,
173 consistent with nuclear pore complexes (Fig. 2A, inset). Within the cytosol, several organelles were
174 visualized by either heavy inner staining with a dim border or weak inner staining.

175 We next tested whether antibodies delivered using a standard immunofluorescence procedure
176 before embedding were also retained in the TREx gel. We stained mouse brain cortex tissue for Bassoon (a
177 marker for both excitatory and inhibitory pre-synaptic active zones), Homer (a marker for the excitatory
178 post-synaptic apparatus), and VGAT (a vesicular GABA transporter in the pre-synaptic compartments of
179 inhibitory synapses). After staining and anchoring with AcX, tissue was expanded with TREx and imaged
180 by light sheet microscopy. Numerous putative excitatory synapses were observed at high density, with
181 clearly separated Bassoon and Homer pre- and post-synaptic staining (Fig. 2B and Supp. Movie 2). VGAT
182 had a more extended staining pattern, consistent with the known distribution of synaptic vesicles throughout
183 pre-synaptic boutons. Elaborately shaped compartments with dense VGAT staining were seen with multiple

synaptic release sites marked by Bassoon (Fig. 2B, inset). As expected, these release sites were not paired with the post-synaptic marker Homer. These results demonstrate the ability of TREx to preserve correct synaptic staining while enabling sub-diffraction limited imaging of large tissue sections.

Subcellular imaging of specific proteins and cellular ultrastructure in cultured cells

We next explored the use of TREx for high-resolution imaging of specific proteins, NHS stains and lipid membranes in cultured cells. For membranes, a custom-synthesized membrane probe compatible with the ExM process has been shown to visualize membrane surfaces in fixed brain tissue (Karagiannis *et al.*, 2019). This probe relies on a peptide-modified lipid tail that intercalates in target membranes and provides opportunities for anchoring to the gel through D-lysines its peptide sequence. We asked whether the commercially available membrane-binding fluorophore-cysteine-lysine-palmitoyl group (mCLING) could also be used for membrane staining and gel anchoring. mCLING has been developed as a fixable endocytosis marker consisting of a fluorophore and a short polypeptide group with one cysteine and seven lysines coupled to a palmitoyl membrane anchor (Revelo and Rizzoli, 2016). Due to the presence of multiple lysines, we hypothesized that mCLING would be compatible with standard ExM anchoring through AcX.

While the standard protocol for mCLING delivery relies on active endocytosis in living cells, we asked if mCLING would stain intracellular membranes more uniformly when added to fixed cells, which would have the added benefit of not perturbing intracellular membrane trafficking by long incubation in live cells. To test this, we fixed activated Jurkat T cells, incubated the fixed cells with mCLING overnight, and proceeded with the TREx protocol. We found that mCLING efficiently intercalates in both the plasma membrane and internal organelles and is retained following standard AcX treatment (Fig. 3A and Supp. Movie 3).

By carefully rendering the imaged volumes we could, with one probe, both appreciate the ruffled morphology of the plasma membrane on top of the flattened part of the cell, and visualize the organelle clustering typical of activated T-cells (Fig. 3A, B). In electron microscopy, distinct morphologies are used to identify organelles. Similarly, we found that we could clearly identify different organelles based on mCLING, suggesting that it could be used for automated segmentation of organelles. Indeed, we found that mitochondria could be readily segmented using a trainable Weka segmentation algorithm (Fig. 3B) (Arganda-Carreras *et al.*, 2017). While the resolution of subcellular structures is limited by the density of mCLING moieties in the membrane, the efficiency of crosslinking to the gel, and the maximum expansion factor, we found TREx allows sufficient single-step expansion to resolve individual mitochondrial cristae, which are known from electron microscopy to be spaced 70 nm apart (Fig. 3C). Although mCLING is

216 thought to be membrane impermeable (due to multiple positively charged amino groups), it readily stained
217 fixed and unpermeabilized cells following extended incubation. Because this approach does not require
218 labeling live cells and is expected to reduce differences in uptake efficiency between intracellular
219 compartments, we used this approach in all subsequent experiments.

220 We next tested if mCLING could also be used to visualize membranes in more complex cell types.
221 To test this, we used differentiated Caco-2 cells grown to form an epithelial monolayer. Using TREx, we
222 could expand the entire monolayer and visualize the membrane using mCLING (Fig. 3D-G and Supp.
223 Movie 4). This enabled us to resolve individual microvilli as hollow membrane protrusions within the dense
224 brush border. In addition, we were able to resolve the elaborate interdigitated cell-cell junctions that could
225 previously only be clearly appreciated using electron microscopy (Drenckhahn and Franz, 1986). The
226 advantage of optical, volumetric imaging is underscored by the fact that we can easily render one dataset
227 in several ways, either resembling scanning electron microscopy to highlight volumetric surface
228 morphology (Fig. 3D), or transmission electron microscopy to explore single planes in more detail (Fig.
229 3E). Together, these data illustrate that TREx can be combined with a commercially available membrane
230 stain to provide rapid volumetric insights into the elaborate membranous architecture of cells.

231 We further tested whether TREx using general membrane stains could be combined with general
232 protein stains and/or antibody stains. U2OS cells transfected with GFP-Sec61β were fixed, treated with
233 mCLING, stained for GFP, and expanded with TREx followed by the NHS stain (Fig. 4A). Because we
234 performed the NHS stain after disruption, we used temperature- and detergent-mediated disruption, rather
235 than proteolytic digestion. We found that secondary antibodies that had been used to stain GFP before
236 gelation withstood this disruption step. We observed a clear degree of overlap between mCLING and NHS,
237 especially in the dense perinuclear region, but we could also identify distinct features of each stain (Fig.
238 4A). Interestingly, we observed strong nucleoplasmic staining in the NHS stain and clear puncta where the
239 imaging plane intersected the nuclear envelope, which presumably are nuclear pores (Fig. 4A). These
240 results demonstrate that general stains for membranes and proteins can be combined with antibody-based
241 labeling to reveal specific proteins in their ultrastructural context.

242 Previously, we have used ExM to study the three-dimensional organization of microtubules (MT)
243 in neurons and T cells (Hooikaas *et al.*, 2020; Jurriens *et al.*, 2020). For high-resolution imaging of the MT
244 cytoskeleton, cells are usually pre-extracted with detergent and glutaraldehyde to remove the soluble pool
245 of tubulin, followed by paraformaldehyde fixation (Tas *et al.*, 2017). This reduces background but does not
246 preserve membranes. We reasoned that the increased expansion of TREx would dilute the background due
247 to soluble tubulin by the expansion factor cubed. Ten-fold expanded microtubules remain diffraction
248 limited in width (i.e., 250-350 nm), so their signal should be reduced only by the expansion factor itself

249 (due to the expansion along their length). Therefore, we wondered whether the resulting relative boost in
250 signal over background would eliminate the need for pre-extraction to enable high-resolution imaging of
251 microtubules in combination with membranes. To test this, we fixed cells expressing GFP-Sec61β without
252 pre-extraction, treated them with mCLING, stained for GFP and tubulin, and then proceeded with TREx
253 (Fig. 4B and Supp. Movie 5). Subsequent confocal microscopy revealed the interplay between microtubules
254 and ER in three dimensions and revealed how other membranous organelles were connected to both
255 structures (Fig. 4C). Thus, TREx facilitates high-resolution three-dimensional mapping of specific
256 cytoskeletal and membranous structures in combination with markers that provide ultrastructural context.

257 **DISCUSSION**

258 We developed Ten-fold Robust Expansion (TREx) in order to expand biological specimens 10-fold
259 in a single round of expansion, without specialized equipment or procedures. In developing this method,
260 we established a framework for assessing gel recipes operating near this apparent limit of single-round
261 expansion. We found that the mechanical performance of gel recipes, i.e. resistance to deformation versus
262 gel expansion factor, varies smoothly with changes in crosslinker. For all high monomer (~3 M total
263 acrylamide and acrylate) gel recipe families, the relation between expansion factor and crosslinker
264 concentration fell close to a common curve. The high radical initiation rate of family B enabled gelation
265 without the inclusion of a crosslinker, suggesting that side reactions and polymer entanglement in these
266 conditions create sufficient effective crosslinks to form a gel. Gel deformation measurements versus
267 expansion factor, though less precise, also show high monomer recipe families falling close to a common
268 curve. Compared to the high monomer families, the original ExM recipe family is less resistant to
269 deformation for a given expansion factor and expands more for a given crosslinker concentration. The factor
270 determining gel properties is not crosslinker concentration in the gel recipe *per se*, but rather the density of
271 effective crosslinks formed between neighboring polymer chains in the gel. This suggests that the original,
272 monomer poor recipe less efficiently incorporates crosslinker molecules as effective polymer crosslinks.
273 This may be because the resulting lower rate of chain extension allows incorporated crosslinker molecules
274 to be re-reacted by the same polymer chain before they can react with neighboring polymers.

275 While the expansion factor of the original ExM recipe can be tuned by varying the crosslinker
276 concentration, it has been shown that increasing the monomer content is required to maintain nanoscale
277 isotropy, using centrioles as a convenient standard reference structure (Gambarotto *et al.*, 2019).
278 Considering gel quality versus expansion factor alone, the high monomer recipe family B derived from the
279 U-ExM recipe allows for a 10-fold expanding gel (at crosslinker concentration of 30 ppm) with a low
280 deformation index of 0.13. However, the high radical initiation rate used in this family (5 ppt APS and
281 TEMED) results in fast gelation. This increases the time sensitivity of mounting the specimen in the gelation

282 chamber and adds an additional challenge for adapting the method to thick tissues requiring extended
283 incubation in the gelation solution. Recipe families C and D solve this problem by reducing initiation rates,
284 at a slight expense of mechanical performance compared with family B. Like family B, family C has a high
285 acrylate content, which might contribute to imaging artifacts due to shrinkage of the sample prior to gelation
286 and inconsistent acrylate purity. Family D reduces the acrylate content by half while retaining similar
287 mechanical performance to family C, especially in the ten-fold expansion regime. Finally, with family E
288 we explored whether increasing the gelation temperature to 50ºC would produce the improved mechanical
289 performance of family B (through increased temperature-dependent radical initiation) without premature
290 gelation at room temperature. However, we found that this reduced the expansion factor and increased
291 susceptibility to experimental variation. Therefore, we based our TREx recipe on recipe family D. The
292 exact crosslinker concentration that produces 10-fold expanding gels was found to vary between labs (i.e.
293 50 ppm in Ashburn, VA, USA versus 90 ppm in Utrecht, The Netherlands, possibly due to differences in
294 gelation chamber design), so we recommend that each lab test a range of crosslinker concentrations between
295 30 and 100ppm using their choice of specimen, gelation chamber, and incubator.

296 We applied TREx to mouse brain tissue slices stained either for specific targets with antibodies, or for total
297 protein distribution with NHS ester dyes. Single round ten-fold expansion with TREx followed by total
298 protein staining was sufficient to reveal densely packed axons and dendrites running through the neuropil,
299 while individual organelles could be resolved within the neuronal soma. The nuclear envelope, along with
300 presumptive nuclear pore complexes, was also clearly resolved. The correct relative localizations of pre-
301 and post-synaptic markers and pre-synaptic neurotransmitter vesicles stained with standard
302 immunohistochemistry were also retained in TREx-expanded tissue slices.

303 We further demonstrated the utility of TREx for the study of cell biology through combinations
304 with several staining modalities in cultured cells, prepared in several culture formats. After a single round
305 of expansion with TREx, the commercially available membrane stain mCLING was able to clearly resolve
306 the internal structure of mitochondria and the detailed pattern of plasma membrane ruffling in activated
307 Jurkat T cells. While these structures would be readily resolved with electron microscopy, we were able to
308 do so in the context of complete cells, enabling concomitant detection and automated segmentation of
309 mitochondria clustered followed T cell activation. Caco-2 cells grown on permeable filters were also
310 successfully stained with mCLING and expanded with TREx to reveal the detailed structure of epithelial
311 microvilli and membrane interdigitations at the contacts of neighboring cells. These structures had
312 previously been known from electron microscopy but were now imaged with ease in the context of entire
313 cell monolayers. Successful application of TREx to filter-cultured Caco-2 cells further demonstrates the

314 robustness of TREx, because we had repeatedly failed to cleanly recover epithelial cultures using standard
315 ExM.

316 Combining mCLING with a total protein stain using NHS esters and an antibody marking the ER
317 in U2OS cells, shows close contacts between ER and other organelles. While the NHS ester and mCLING
318 staining patterns were similar in their overall contours, some clear differences in staining patterns were
319 noted, including the presence of presumptive nuclear pore complexes in the NHS ester channel. The strong
320 overlap between NHS ester and mCLING stains was not unexpected, given the reactivity of NHS esters
321 towards both unreacted lysines in the mCLING molecule and antibodies. However, the extent to which
322 NHS ester staining is truly unbiased over all proteins and how it may be modulated by the local environment
323 awaits further exploration.

324 In U2OS cells, TREx retained anti-tubulin antibody stain with high efficiency, maintaining
325 continuous microtubules with high signal-to-noise ratio after 1000-fold volumetric expansion. Combined
326 staining for ER and all membranes revealed close appositions along microtubules, ER and presumptive
327 mitochondria. In unexpanded cells, high quality antibody staining for microtubules requires monomeric
328 tubulin to be removed with a pre-extraction step, which destroys membranes and extracts other proteins.
329 For specimens expanded with TREx, this is not necessary as the monomeric tubulin signal is diluted 1000-
330 fold volumetrically, while the diameter of an expanded microtubule is still below the diffraction limit, so
331 the signal is only diluted by the the 10-fold linear expansion factor. This 1000-fold volumetric dilution is
332 also what enables the use of dense protein stains such as NHS ester dyes, which in unexpanded specimens
333 would be too dense to resolve any meaningful structure.

334 In summary, by systematically exploring the ExM recipe space we established a novel recipe using
335 standard ExM reagents that can be rapidly adopted by other labs. TREx allows for ten-fold expansion of
336 both thick tissue slices and cells in a single expansion step and has applications in tissue and high-resolution
337 subcellular imaging. Importantly, TREx of antibody-stained samples can be combined with off-the-shelf
338 small molecule stains for both membranes and total protein to provide ultrastructural context.

339 **ACKNOWLEGDMENTS**

340 We are grateful to Sven van IJzendoorn (UMCG) and Wilco Nijenhuis (UU) for providing the Caco2
341 monolayer samples. L.C.K. is supported by the European Research Council (ERC Consolidator Grant
342 819219). B.M. and P.W.T are supported by the Howard Hughes Medical Institute (HHMI).

343 **REFERENCES**

344 Arganda-Carreras, I. *et al.* (2017) 'Trainable Weka Segmentation: A machine learning tool for
345 microscopy pixel classification', *Bioinformatics*. doi: 10.1093/bioinformatics/btx180.

346 Chang, J.-B. *et al.* (2017) 'Iterative expansion microscopy', *Nature Methods*. Nature Research, 14(6), pp.
347 593–599. doi: 10.1038/nmeth.4261.

348 Chen, F., Tillberg, P. W. and Boyden, E. S. (2015) 'Expansion microscopy', *Science (New York, N.Y.)*,
349 347(6221), pp. 543–548. doi: 10.1126/science.1260088.

350 Drenckhahn, D. and Franz, H. (1986) 'Identification of actin-, α-actinin-, and vinculin-containing plaques
351 at the lateral membrane of epithelial cells', *Journal of Cell Biology*. doi: 10.1083/jcb.102.5.1843.

352 Gambarotto, D. *et al.* (2019) 'Imaging cellular ultrastructures using expansion microscopy (U-ExM)',
353 *Nature Methods*. Nature Publishing Group, 16(1), pp. 71–74. doi: 10.1038/s41592-018-0238-1.

354 Gao, M. *et al.* (2018) 'Expansion Stimulated Emission Depletion Microscopy (ExSTED)'. doi:
355 10.1021/acsnano.8b00776.

356 Gao, R. *et al.* (2019) 'Cortical column and whole-brain imaging with molecular contrast and nanoscale
357 resolution', *Science*. American Association for the Advancement of Science, 363(6424). doi:
358 10.1126/science.aau8302.

359 Gustafsson, M. G. L. (2000) 'Surpassing the lateral resolution limit by a factor of two using structured
360 illumination microscopy', *Journal of Microscopy*. John Wiley & Sons, Ltd, 198(2), pp. 82–87. doi:
361 10.1046/j.1365-2818.2000.00710.x.

362 Halpern, A. R. *et al.* (2017) 'Hybrid Structured Illumination Expansion Microscopy Reveals Microbial
363 Cytoskeleton Organization', *ACS Nano*, 11(12), pp. 12677–12686. doi: 10.1021/acsnano.7b07200.

364 Hell, S. W. and Wichmann, J. (1994) 'Breaking the diffraction resolution limit by stimulated emission:
365 stimulated-emission-depletion fluorescence microscopy', *Optics Letters*. The Optical Society, 19(11), p.
366 780. doi: 10.1364/ol.19.000780.

367 Hooikaas, P. J. *et al.* (2020) 'Kinesin-4 kif21b limits microtubule growth to allow rapid centrosome

368 polarization in t cells', *eLife*. eLife Sciences Publications Ltd, 9, pp. 1–75. doi: 10.7554/ELIFE.62876.

369 Jurriens, D. *et al.* (2020) 'Mapping the neuronal cytoskeleton using expansion microscopy', in *Methods in*
370 *Cell Biology*. doi: 10.1016/bs.mcb.2020.04.018.

371 Karagiannis, E. D. *et al.* (2019) 'Expansion Microscopy of Lipid Membranes', *bioRxiv*. doi:
372 10.1101/829903.

373 Ku, T. *et al.* (2016) 'Multiplexed and scalable super-resolution imaging of three-dimensional protein
374 localization in size-adjustable tissues', *Nature Biotechnology*, 34(9), pp. 973–981. doi: 10.1038/nbt.3641.

375 M'Saad, O. and Bewersdorf, J. (2020) 'Light microscopy of proteins in their ultrastructural context',
376 *Nature Communications*. doi: 10.1038/s41467-020-17523-8.

377 Mao, C. *et al.* (2020) 'Feature-rich covalent stains for super-resolution and cleared tissue fluorescence
378 microscopy', *Science Advances*. American Association for the Advancement of Science, 6(22), p.
379 eaba4542. doi: 10.1126/sciadv.aba4542.

380 Okay, O. (2009) 'General Properties of Hydrogels', in Gerlach G., A. K. (ed.) *Hydrogel Sensors and*
381 *Actuators. Springer Series on Chemical Sensors and Biosensors (Methods and Applications)*. vol. 6.
382 Springer, Berlin, Heidelberg, pp. 1–14. doi: 10.1007/978-3-540-75645-3_1.

383 Revelo, N. H. and Rizzoli, S. O. (2016) 'The membrane marker mCLING reveals the molecular
384 composition of trafficking organelles', *Current Protocols in Neuroscience*. doi:
385 10.1002/0471142301.ns0225s74.

386 Rust, M. J., Bates, M. and Zhuang, X. W. (2006) 'Sub-diffraction-limit imaging by stochastic optical
387 reconstruction microscopy (STORM)', *Nat Methods*, 3(10), pp. 793–795. doi: Doi 10.1038/Nmeth929.

388 Tas, R. P. *et al.* (2017) 'Differentiation between Oppositely Oriented Microtubules Controls Polarized
389 Neuronal Transport', *Neuron*. doi: 10.1016/j.neuron.2017.11.018.

390 Tillberg, P. W. *et al.* (2016) 'Protein-retention expansion microscopy of cells and tissues labeled using
391 standard fluorescent proteins and antibodies', *Nature Biotechnology*. Nature Publishing Group, 34(9), pp.
392 987–992. doi: 10.1038/nbt.3625.

393 Truckenbrodt, S. *et al.* (2018) 'X10 expansion microscopy enables 25-nm resolution on conventional
394 microscopes.', *EMBO reports*. EMBO Press, 19(9), p. e45836. doi: 10.15252/embr.201845836.

395 Truckenbrodt, S. *et al.* (2019) 'A practical guide to optimization in X10 expansion microscopy', *Nature*
396 *Protocols*. doi: 10.1038/s41596-018-0117-3.

397 Xu, H. *et al.* (2019) 'Molecular organization of mammalian meiotic chromosome axis revealed by
398 expansion STORM microscopy', *Proceedings of the National Academy of Sciences of the United States of*
399 *America*. National Academy of Sciences, 116(37), pp. 18423–18428. doi: 10.1073/pnas.1902440116.

400 Yu, C.-C. (Jay) *et al.* (2020) 'Expansion microscopy of C. elegans', *eLife*, 9. doi: 10.7554/eLife.46249.

401 Zhang, Y. S. *et al.* (2016) 'Hybrid Microscopy: Enabling Inexpensive High-Performance Imaging
402 through Combined Physical and Optical Magnifications', *Scientific Reports*. Nature Publishing Group,
403 6(1), p. 22691. doi: 10.1038/srep22691.

404 Zwettler, F. U. *et al.* (2020) 'Molecular resolution imaging by post-labeling expansion single-molecule
405 localization microscopy (Ex-SMLM)', *bioRxiv*. Cold Spring Harbor Laboratory, p. 2020.03.12.988923.
406 doi: 10.1101/2020.03.12.988923.

407

408 **MATERIAL AND METHODS**

409 **Gelation chambers for recipe space exploration**

410 A glass slide served as the bottom piece of each gelation chamber. Four strips of 250 µm-thick adhesive
411 silicone material (Digikey cat# L37-3F-320-320-0.25-1A), ~3 mm wide and running the width of the slide,
412 were adhered to the slide to partition it into three separate chambers, each ~12 mm wide. A plus-charged
413 glass slide was placed over the silicone strips to form the top of the gelation chamber and held in place with
414 tape. Two sides of each chamber were open to air, providing a convenient fill port for adding ~100 uL of
415 monomer solution after chamber construction.

416 **Gel synthesis and characterization for recipe space exploration**

417 Sodium acrylate was made by neutralizing acrylic acid (Sigma, 147230) by adding NaOH until the pH
418 reached the range of 7.5-8. Initial neutralization (until pH ~7) was done with 10 N NaOH on ice and using
419 a fume hood to avoid acrylic acid vapor. Neutralization was done in a volume of water calculated to yield
420 a final concentration of 4 M sodium acrylate. The gel recipes for each family contained 1xPBS and the
421 amounts of acrylamide (Sigma, A4058), sodium acrylate, and initiator (APS, Sigma, A3678) indicated in
422 Fig. 1A. Each gel recipe contained the same amount of TEMED (Sigma, T7024) as APS. For each recipe
423 family, gelation solution with crosslinker withheld (but including APS and TEMED) was premixed on ice,
424 in one tube for each recipe family. This solution was then split into six tubes and mixed with serial dilutions
425 of crosslinker (bisacrylamide, Sigma, M1533) to arrive at final crosslinker concentrations of 1 ppt, 300,
426 100, 30, and 10 ppm, and 0. Complete gelation solution thus obtained was pipetted into gelation chambers
427 and incubated at 50 ºC for 1 hour or 37 ºC for 2 hours. Gels were then cooled for 15 minutes at room
428 temperature and chamber tops carefully removed. Gels typically remained stuck exclusively to the top (plus
429 charged) slide. Specimens of each gel were taken with a 6 mm biopsy punch, taking care to avoid material
430 within ~2 mm of the chamber edges (due to oxygen exposure during gelation). Excess gel was scrapped
431 away with a razor blade. A few drops of distilled water were pipetted onto each gel to help release them
432 from the glass slide. Each 6 mm gel specimen was gently released from the slide with a razor blade, placed
433 in a 9 cm Petri Dish and expanded by washing with excess water 2x 15 minutes followed by 2x 1 hour.
434 Diameters of expanded gels were measured and divided by 6 mm to obtain the expansion factor. A semi-
435 circle 25 mm in diameter was punched from each gel using a cookie cutter. Semi-circular gel punches were
436 placed in a plastic tray, which was stood up on end so that the gel stood upright on its curved side. For stiff
437 gels, the top edge remained straight and level while for weak gels the top edge deformed under the force of
438 gravity to form a curve. Each gel was photographed, with a ruler positioned for scale. Using image J, each

439 top edge was described by seven manually chosen points, which were then fit to a circle. This best-fit circle
440 was used to calculate the vertical deviation of the gel corners, which was divided by the gel radius to obtain
441 the deformation index.

442 **TREx gelation solution**

443 Sodium acrylate was either purchased (Sigma, 408220) or made by neutralizing acrylic acid by adding
444 NaOH until the pH reached the range of 7.5-8. Initial neutralization (until pH ~7) was done with 10N NaOH
445 on ice and using a fume hood to avoid acrylic acid vapor. TREx gelation solution contains 1.1 M sodium
446 acrylate, 2.0 M acrylamide (AA), 50 ppm (for tissue slices prepared at Janelia) or 90ppm (for cultured cells
447 prepared at University of Utrecht) N,N'-methylenebisacrylamide (bis), PBS (1x), 1.5 ppt APS, 1.5 ppt
448 TEMED, and (optionally, for thick tissue slices) 15 ppm 4HT. Monomer solution was made by combining
449 all components of gelation solution except APS, TEMED, and 4HT. Monomer solution may be aliquoted
450 and stored at -20ºC, but must be thawed at room temperature and thoroughly vortexed before use to
451 redissolve any acrylamide crystals that may have precipitated at low temperature before freezing. 4HT,
452 TEMED, and APS were added to monomer solution to produce gelation solution directly before use.

453 **Tissue experiments**

454 Mice were transcardially perfused with ice cold 4% formaldehyde in 100 mM sodium phosphate buffer, pH
455 7.4. Brains were dissected out and post-fixed in 4% formaldehyde overnight at 4ºC, followed by washing
456 with PBS (1x) and slicing at 100 µm by vibratome. Slices were optionally stained with standard IHC
457 procedures. Primary antibodies (Chicken anti Bassoon Synaptic systems cat#141016, RRID:AB_2661779;
458 Rabbit anti Homer abcam cat#97593, RRID:AB_10681160; Ms IgG3 VGAT SySy cat#131011,
459 RRID:AB_887872) were used at 1:300 dilution in PBS with 0.1% Triton and 2% BSA (PBT) overnight at
460 4°C. Sections were washed 3x 30min in PBT and given at least 6h in secondary antibodies 1:500 in PBT at
461 room temperature (Goat Anti-Rabbit alexa 488 abcam cat#150077, RRID:AB_2630356; Goat anti-Mouse
462 IgG3 alexa 594 invitrogen cat# A-21155, RRID: AB_2535785; Goat anti chicken CF633 biotium
463 cat#20126, RRID: AB_10852831). After 3x 30min washes in PBS, slices were treated with 10 µg/mL AcX
464 in PBS for 1 hour at room temperature, followed by rinsing with PBS. Slices were incubated with TREx
465 gelation solution (using 50ppm bis, and with 4HT added up to 15ppm), for 20min on ice, with shaking.
466 Following incubation on ice, each tissue specimen was placed on a glass slide at room temperature. Four
467 dabs of vacuum grease were applied to the slide, with each dab at least several mm from the tissue specimen.
468 A coverslip was placed over the tissue and vacuum grease dabs, and pressed down until contacting the
469 tissue, taking care not to let the tissue slide around on the slide. The vacuum grease served to hold the

470 assembly in place, thus forming the gelation chamber. Gelation solution was pipetted into the chamber from
471 the side to fully surround the tissue. The chamber was incubated at 37 ºC for 1 hour to complete gelation.
472 Following embedding, excess gel was removed with a razor blade, and gelled slices were recovered into
473 disruption buffer (5% SDS, 200 mM NaCl, 50 mM Tris pH 7.5), using a razor blade to gently release them
474 from the glass slide. Gels were incubated at 80 ºC for 3 hours, followed by washing in water once and PBS
475 several times to remove residual SDS. Slices were optionally stained with BODIPY-FL NHS at 10-20 µM
476 (and optionally DAPI) in PBS for 1 hour at room temperature. Disrupted slices were placed in glass bottom
477 6-well plates and washed in milliQ water 3x 15 minutes followed by 2x 1 hour to fully expand. Gels with
478 total protein stain were imaged by confocal microscopy using a Zeiss LSM 800 with 40x/1.2NA, water
479 immersion objective. Gels with synaptic antibody stains were imaged on a Zeiss Z1 lightsheet microscope
480 with 10x/0.3NA illumination objectives and 20x/1.0NA water immersion detection objective. Scale bar
481 represent the expanded size divided by the approximate expansion factor of 10.

482 **Cell culture and T cell activation**

483 Jurkat T cells (clone E6.1) were grown in RPMI 1640 medium w/ L-Glutamine (Lonza) supplemented with
484 9% Fetal Bovine Serum and 1% penicillin/streptomycin. For T cell activation, 18 mm #1.5 coverslips
485 (Marienfeld, 107032) were coated with Poly-D-Lysine (Thermo Fisher Scientific, A3890401), washed with
486 phosphate buffered saline (PBS) and incubated overnight at 4 °C with a mouse monoclonal anti-CD3 (clone
487 UCHT1, StemCell Technologies, #60011) 10 µg/mL in PBS. Cells were spun down for 4 minutes at 1000
488 rpm and resuspended in fresh, prewarmed RPMI 1640 medium, after which cells were incubated on the
489 coated coverslips for 3 minutes prior to fixation. U2OS cells were cultured in DMEM medium
490 supplemented with 9% Fetal Bovine Serum and 1% penicillin/streptomycin. U2OS cells were transfected
491 with GFP-Sec61β (Addgene, 15108) using FuGENE6 (Promega). Caco2-BBE cells (a gift from S.C.D. van
492 IJzendoorn, University Medical Center Groningen, The Netherlands) were maintained in DMEM
493 supplemented with 9% FBS, 50 µg/µl penicillin/streptomycin and 2 mM L-glutamine. For imaging, cells
494 were seeded on 6.5 mm Transwell filters (3470; Corning) at a density of 1 x 10^5/cm^2 and cultured for 10-
495 12 days to allow for spontaneous polarization and brush border formation.

496 **Immunofluorescence, mCLING treatment and antibodies**

497 For all experiments, cells were fixed for 10 minutes with pre-warmed (37 °C) 4% paraformaldehyde + 0.1%
498 glutaraldehyde in PBS. For visualization of lipid membranes, cells were washed twice in PBS after fixation
499 and incubated in 5 µM either mCLING-Atto647N (Synaptic Systems, 710 006AT1) or mCLING-Atto488
500 (Fig. 3C, Synaptic Systems, 710 006AT3) in PBS overnight at RT. The following day, cells were fixed a

501 second time with pre-warmed (37 °C) 4% paraformaldehyde + 0.1% glutaraldehyde in PBS. Next, cells
502 were washed with PBS and permeabilized using PBS + 0.2% Triton X-100. Epitope blocking and antibody
503 labeling steps were performed in PBS + 3% BSA. For immunofluorescence staining, we used a rabbit
504 monoclonal antibody against α-tubulin (clone EP1332Y, Abcam, ab52866) and a chicken polyclonal
505 antibody against GFP (Aves Labs, GFP-1010) in combination with goat anti-rabbit IgG (H+L) Alexa Fluor
506 594 (Molecular Probes, a11037) and goat anti-chicken IgY (H+L) Alexa Fluor 488 (Molecular Probes,
507 a11039), respectively.

508 **TREx protocol and NHS staining**

509 For TREx Microscopy, samples were treated with 0.1 mg/mL acryloyl X-SE (AcX) (Thermo Fisher,
510 A20770) in PBS overnight at RT. TEMED and APS were added to monomer solution (1.5 ppt each) to
511 produce gelation solution. 170 µL of gelation solution was transferred to a silicone mold with inner diameter
512 of 13 mm (Sigma-Aldrich, GBL664107) attached to a parafilm-covered glass slide, with the sample put
513 cell-down on top to close off the gelation chamber. The sample was directly transferred to a 37 °C incubator
514 for 1 hour to fully polymerize the gel. All gels excluding samples that were processed for subsequent NHS
515 ester staining were transferred to a 12-well plate and digested with 7.5 U/mL Proteinase-K (Thermo Fisher,
516 EO0491) in TAE buffer (containing 40 mM Tris, 20 mM acetic acid and 1 mM EDTA) supplemented with
517 0.5% Triton X-100, 0.8 M guanidine-HCl, and DAPI for 4 hours at 37 °C. The gel was transferred to a Petri
518 dish, water was exchanged 2x 30 minutes and the sample was left in milliQ water to expand overnight.

519 For NHS-staining, gels were first treated in disruption buffer containing 200 mM SDS, 200 mM NaCl and
520 50 mM Tris pH 6.8 for 1.5 hours at 78°C. Gels were washed twice for 15 minutes in PBS and incubated
521 with 20 µg/mL Atto 594 NHS ester (Sigma-Aldrich, 08471) in PBS prepared from a 20 mg/mL stock
522 solution in DMSO for 1 hour at RT with shaking. After staining, gels were washed with excess of PBS,
523 transferred to a Petri dish, and expanded overnight. Prior to imaging the cells were trimmed using a scalpel
524 blade to fit in a Attofluor Cell Chamber (Molecular probes A-7816).

525 **Image acquisition and analysis**

526 All cultured cell ExM images were acquired using a Leica TCS SP8 STED 3X microscope equipped with
527 a HC PL APO 86x/1.20W motCORR STED (Leica 15506333) water objective. A pulsed white laser (80
528 MHz) was used for excitation. The internal Leica GaAsP HyD hybrid detectors were used with a time gate
529 of $1 \leq tg \leq 6$ ns. The set-up was controlled using LAS X and run without stimulated emission depletion
530 (STED).

All data processing and analysis was done using ImageJ and Arivis.

For Fig. 2A, raw data was drift corrected using Huygens Professional (SVI) and imported into ImageJ where a sum-projection of 2 planes (z-spacing: 0.8 µm) was made. Fig. 2B is a maximum projection of 2 planes (z-spacing: 0.38 µm) and indicated zoom is a volumetric render of the raw data in Arivis. For Fig. 3A, raw data was imported in Arivis, a Discrete Gaussian Filter with smoothing radius of 2 was applied and this dataset was used for volumetric renders and clipping. Gamma was adjusted manually to increase visibility of plasma membrane ruffles and intracellular organelles in the same view. For Fig. 3B, the same raw dataset was imported in ImageJ and a sum-projection of 3 planes (z-spacing: 0.35 µm) around the plane of the immunological synapse was segmented for mitochondria using the trainable Weka segmentation plugin in ImageJ. Fig. 3C is a sum-projection of 3 planes (z-spacing 0.35 µm). The linescan in Fig. 3C was generated using ImageJ and processed using Graphpad Prism 8.

For Fig. 3D, raw data was imported in Arivis, a Discrete Gaussian Filter with smoothing radius of 2 was applied and this dataset was volumetrically rendered with the opacity mapped to the z-axis. For Fig. 3E, raw data was imported in ImageJ and a running sum projection of 5 slices (z-spacing 0.35 µm) was generated using the RunningZProjector plugin and gamma was adjusted manually to increase intracellular contrast. The resulting image was imported into Arivis for volumetric rendering. Fig. 3F and G are maximum projections of 3 planes (z-spacing: 0.35 µm) and respective zooms.

Fig 4A is a maximum projection of 3 planes (z-spacing: 0.35 µm). For Fig 4B, raw data was imported into Arivis, a Discrete Gaussian Filter with smoothing radius of 2 was applied and this dataset was used for volumetric renders and clipping. Fig 4C is a sum projection of 3 slices (z-spacing 0.35 µm) of the same raw data as Fig. 4B and was processed using ImageJ.

557 **FIGURES**

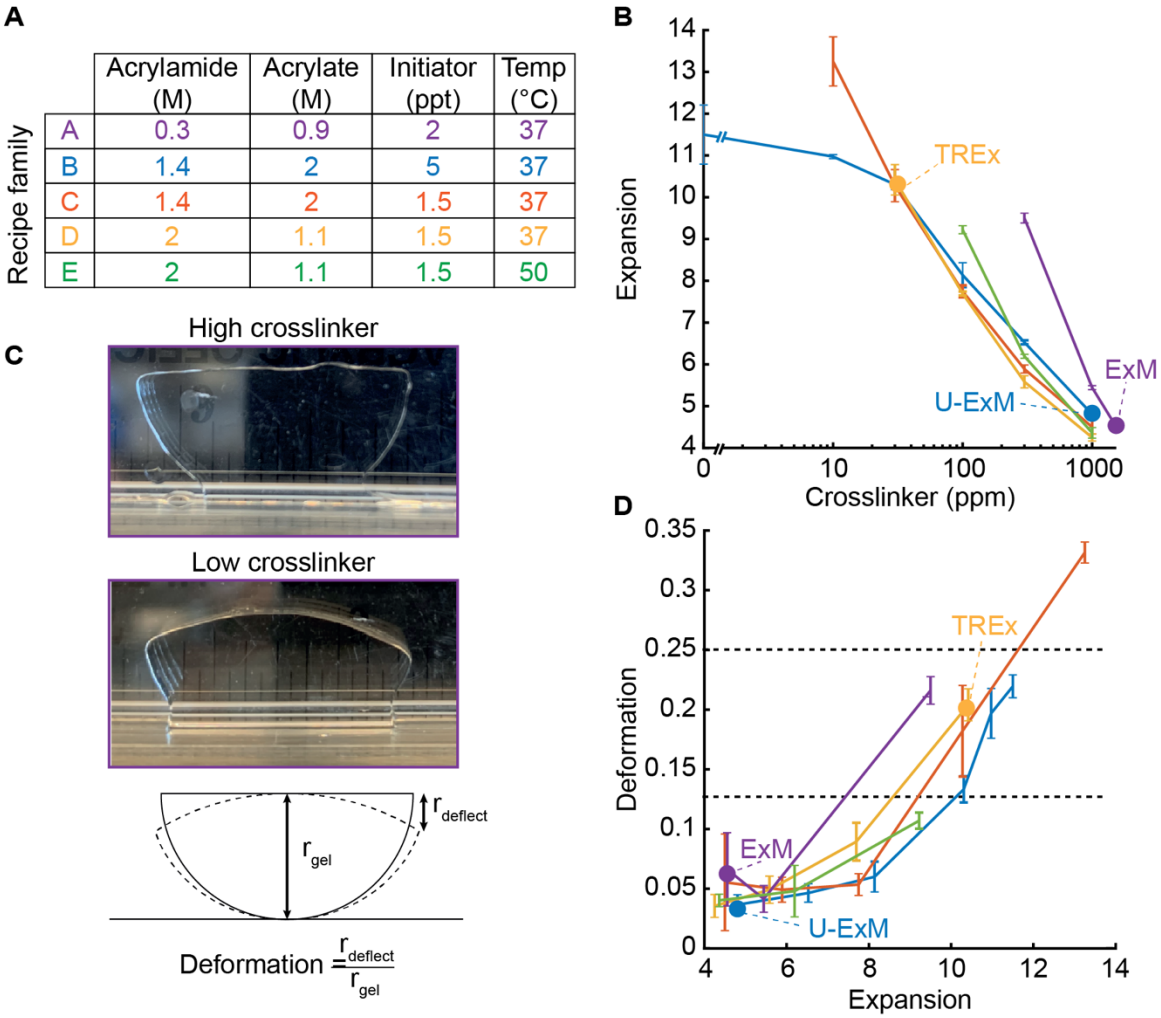

558

559 **FIGURE 1: Development of TREx gel recipe**

560 A) Parameters of gel recipe families explored, including component concentrations and gelation
561 temperature. Each family was characterized by keeping these conditions constant while systematically
562 varying the crosslinker concentration.

563 B) Expansion factor (mean ±s.d., n=3) versus crosslinker concentration (log scale) for each gel recipe
564 family without biological specimens. Line colors correspond to recipe families as in 1A. Specific recipes
565 (with specific crosslinker concentrations) are indicated as follows: filled purple dot - original ExM recipe,
566 blue dot - UltraExM, and yellow dot - TREx. All recipe families were tested with crosslinker concentrations
567 of 0, 10, 30, 100, 300, 1000 ppm, plus an addition condition with 1500 ppm for family A corresponding to
568 the original ExM recipe. Only conditions in which gels formed are plotted.

569 C) Definition of gel deformation index. Example gels from recipe family A with high crosslinker and low
570 deformation (top panel, 1.5 ppt), and low crosslinker and high deformation (middle panel, 300 ppm).
571 Bottom panel, schematic illustrating deformation index measurement.

572 D) Deformation index (mean ±s.d., n=3) versus expansion factor for each gel recipe family without
573 biological specimens, with line colors and dots corresponding to specific recipes as in 1A and 1B.
574 Horizontal grey lines indicate thresholds for gels with mechanical quality deemed perfect (deformation <
575 0.125) and acceptable (deformation < 0.25). Ideal recipes would occupy the lower right quadrant,
576 corresponding to high expansion and low deformability.

577

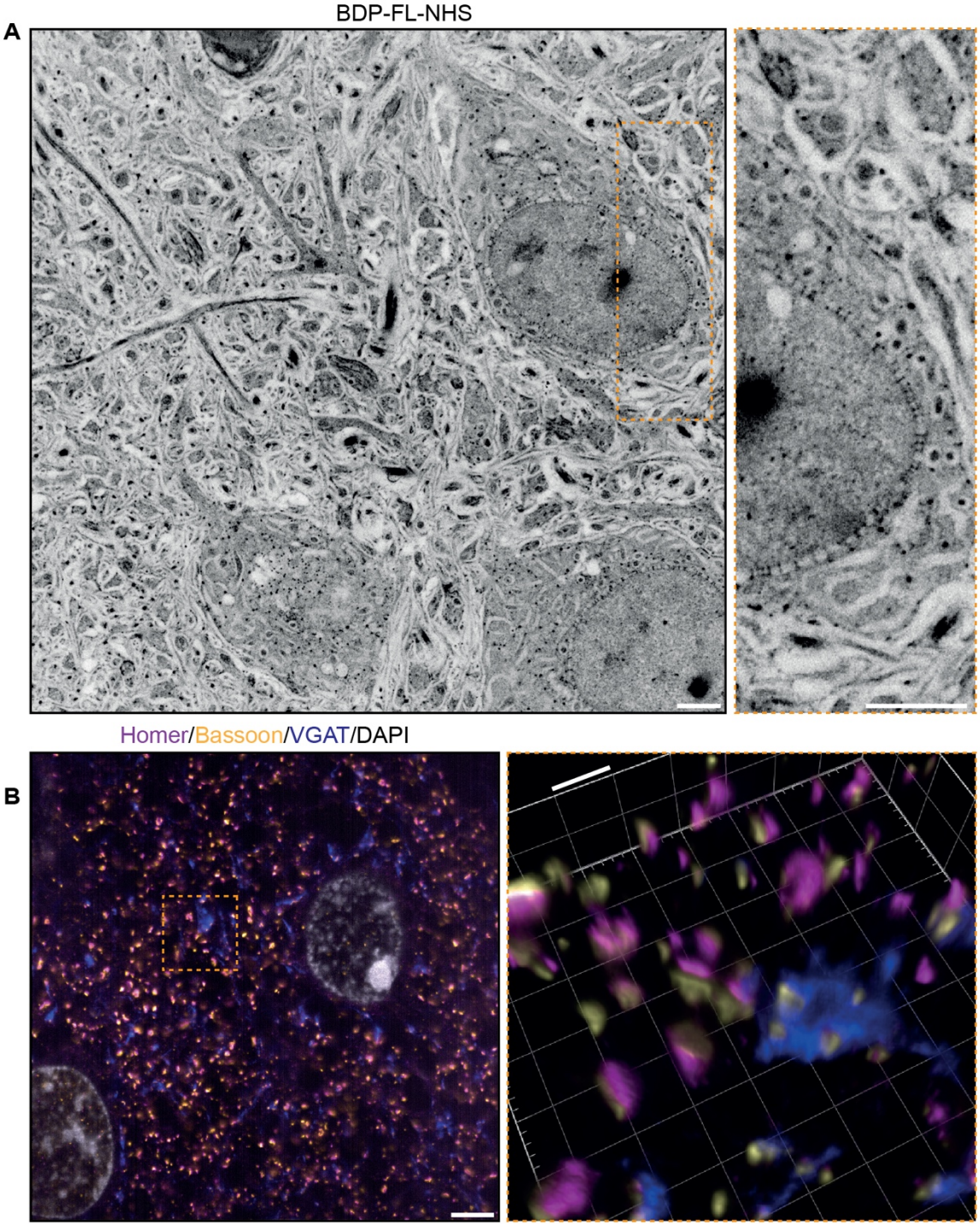

578

579 **FIGURE 2: TREx in mouse brain tissue slices**

580 A) Mouse brain tissue (cortex) expanded using TREx, stained for total protein content with BODPIY-FL
581 NHS, and imaged by confocal microscopy. Displayed contrast is inverted to show dense stained regions as

582 dark. Inset, zoom-in showing nuclear envelope with densely stained structures spanning the nuclear
583 envelope, consistent with nuclear pore complexes.

584 B) Mouse brain tissue (cortex) stained with antibodies against (purple) homer, (yellow) bassoon, and (blue)
585 VGAT, and DAPI (grey), and expanded using TREx. Inset, zoom-in showing paired bassoon and homer-
586 rich structures, consistent with excitatory synapses and complex structured pre-synaptic vesicle pool
587 marked by VGAT bearing several release sites marked by bassoon.

588 Scale bars (corrected to indicate pre-expansion dimensions): main ~2 µm, zooms ~400 nm

589

590

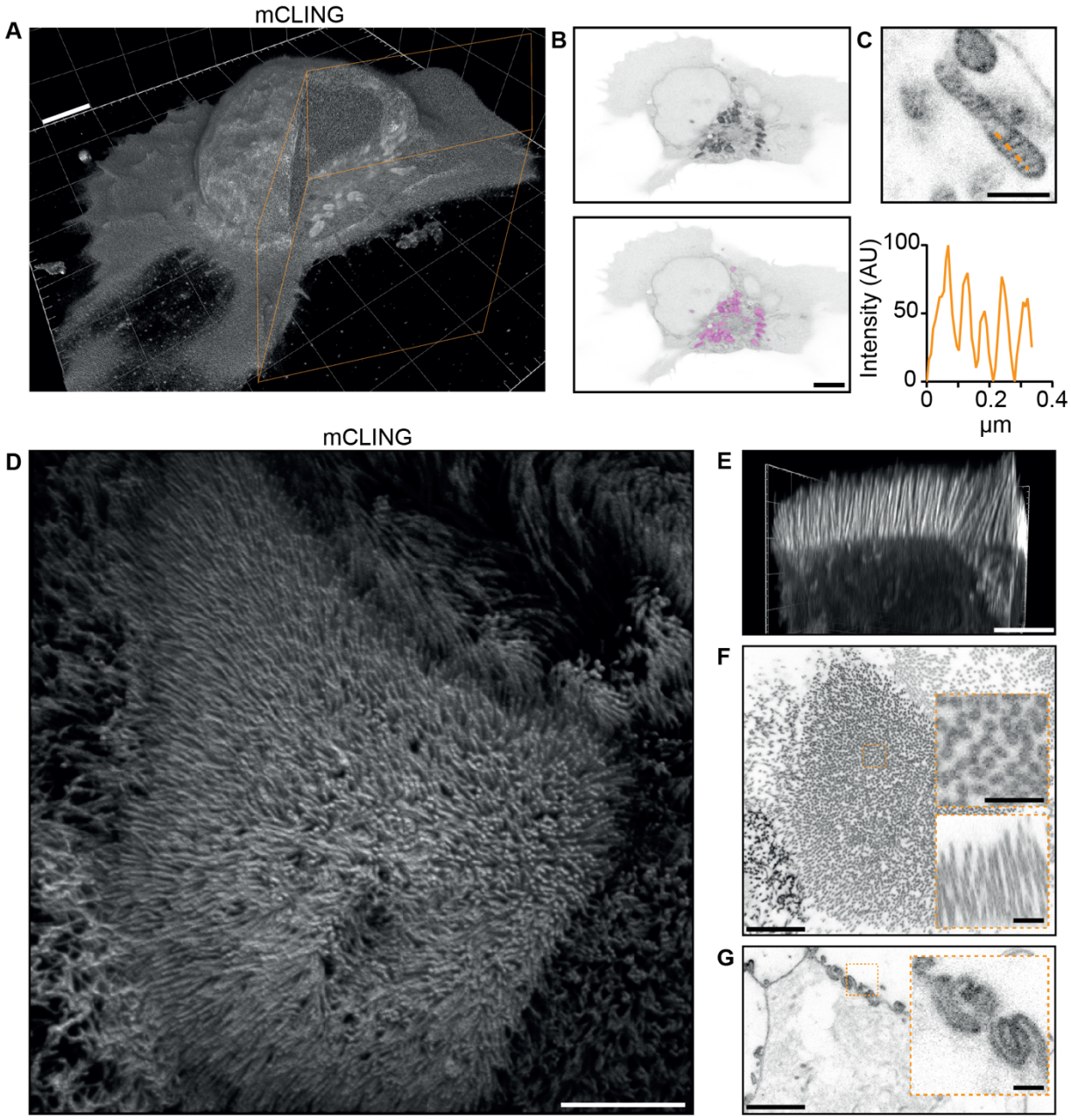

591

592 **FIGURE 3: TREx can be used to visualize the ultrastructure of cellular membranes**

593 A) Volumetric render of Jurkat T cell activated on anti-CD3 coated coverslip fixed and stained using
594 mCLING. Colored clipping planes indicate portion clipped out to reveal intracellular detail.

595 B) Immunological synapse of activated T cell stained with mCLING in (A) revealing organelle clustering
596 at the immunological synapse. Below: mitochondria segmented using the trainable Weka segmentation
597 algorithm indicated in magenta.

598 C) Representative example of mitochondrion in T cells visualized with mCLING. Line profile along the
599 orange dashed line indicates mitochondrial cristae.

600 D) Volumetric projection of Caco2 monolayer apical brush border as seen from above looking down on the
601 cells.

602 E) Volumetric side projection of a portion of the cell shown in D as seen from the side.

603 F) Brush border x, y plane of the cell shown in D, with zooms revealing hollow microvilli.

604 G) Similar to F, representative plane below the apical surface revealing highly interdigitated cell-cell
605 contacts.

606 Scale bars (corrected to indicate pre-expansion dimensions): A, B, D, E ~2 µm, C ~500 nm, F and G main
607 ~2 µm and zooms ~500 nm

608

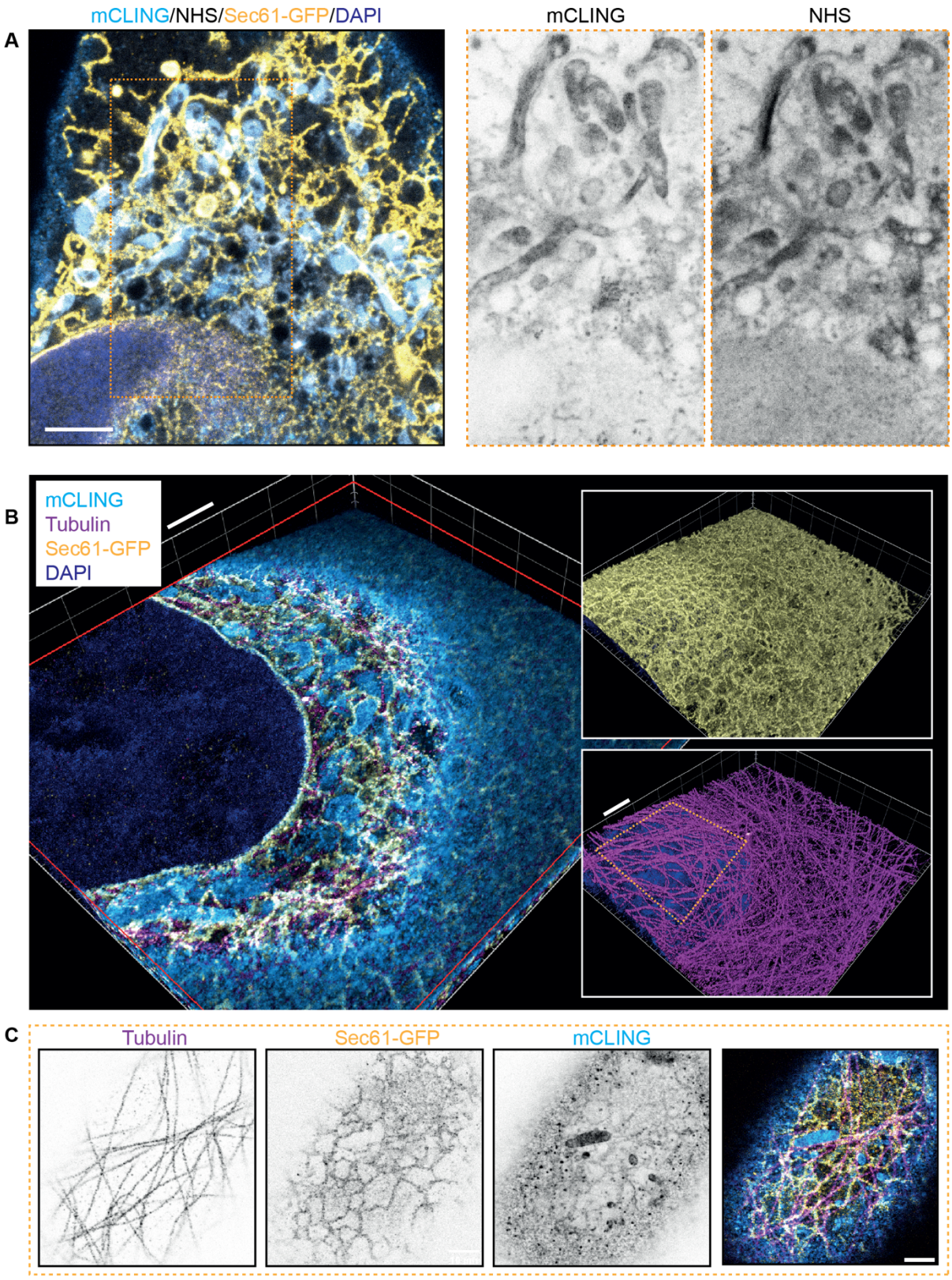

FIGURE 4: TREx Microscopy can combine antibody-based staining with NHS ester total protein

611 **stain to provide cellular context**

612 A) Merged plane of expanded U2OS cell expressing GFP-Sec61β stained for mCLING, GFP, NHS ester
613 and DAPI. Single planes of mCLING and NHS ester are displayed in inverted contrast.

614 B) Volumetric render of U2OS cell expressing GFP-Sec61β Sec61β stained for mCLING, GFP and tubulin.
615 Top portion of cell is clipped with clipping plane indicated in red. Volumetric render of entire volume for
616 GFP and tubulin in insert A and B, respectively.

617 C) Single planes displayed in inverted contrast of the top of cell in B revealing the tight spatial organization.

618 Scale bars (corrected to indicate pre-expansion dimensions): A, C ~1 µm, B ~2 µm

619

620 **SUPPLEMENTAL MOVIES**

621 **Supplemental Movie 1:** Z-stack of Fig. 2A

622 **Supplemental Movie 2:** 3D render of Fig. 2B

623 **Supplemental Movie 3:** 3D render of Fig. 3A

624 **Supplemental Movie 4:** 3D render of Fig. 3D

625 **Supplemental Movie 5:** 3D render of Fig. 4B